RAA 2021 Vol. **21** No. **4**, 79(14pp) doi: 10.1088/1674-4527/21/4/79

http://www.raa-journal.org *http://iopscience.iop.org/raa*

Research in Astronomy and Astrophysics

Solar radio filtering algorithm based on improved long short-term memory

Qing-Fu Du, Qiao-Man Zhang, Xin Li and Chang-Lin Gao

School of Mechanical, Electrical & Information Engineering, Shandong University, Weihai 264209, China; *201836556@mail.sdu.edu.cn*

Received 2020 June 25; accepted 2020 September 21

Abstract The effective observation of burst events in solar radio research has been impeded by various interference signals, especially interference signals with a wide frequency range and high intensity, as they can partially or completely obscure the observation of burst events. Image processing methods that directly remove the interference signal channels and subtract the average of the interference signal channel are not suitable for processing all types of interference signals. This paper proposes the use of a specific kind of recurrent neural networks, called long short-term memory networks, to predict the value of the radio frequency interference signals with high intensity of the burst event in the solar radio spectrum. The predicted interference can then be removed in accordance with the principle that signals can be linearly added. Therefore, predicted value is subtracted from the data containing the burst event signals and the RFI signals (The radio frequency interference signals to be processed in this article refer to the signal of the broadcast signal that can be received in the frequency range, the signal transmitted by the mobile phone, and the signal transmitted by the sea vessel, and the like) to remove the interference. Then, in order to reduce the error caused by the stepwise prediction in the network and further improve the prediction accuracy, this paper analyzes the characteristics of the value of the radio interference and applies the digital mapping method to convert the prediction problem into the classification problem in the time series. The experimental results show that the proposed method can effectively remove the radio interference in the solar spectrum and clearly show the burst events.

Key words: Sun: radio radiation — methods: data analysis — techniques: image processing

1 INTRODUCTION

Solar activity is closely related to our daily lives, so solar radio has become an important area in astrophysics research. In particular, the study of the solar radio burst process, carrying important information, not only helps to explain the physical process of the relevant plasma changes, but can also be used to find the law of energy change and analyze important physical phenomena such as material motion (Cheng 2018). In order to better study the detailed structure of solar radio bursts, the project team established a solar radio dynamic spectrometer with high time resolution and high frequency resolution at the Chashan Solar Observatory.

The Chashan Solar Observatory faces the sea and is far away from the town, which avoids a complicated communication environment and greatly reduces the radio frequency interference (RFI). However, there are still some RFI signals and other electromagnetic interference in the meter band. These interference signals seriously affect the observation and analysis of solar radio burst events. In particular, when the interfering signals frequency is wide (the radio interference with a bandwidth greater than or equal to 2MHz), and the signal intensity is greater than the intensity of the solar radiation flow, the interference can directly cover the burst event, so it is necessary to take anti-interference measures.

Common filtering countermeasures for solar radio spectrograms are divided into hardware processing and software processing methods. In hardware processing methods, Xu et al. use the spatial selectivity of the antenna to attenuate various interferences from the ground, use shielding, grounding, and amplifiers whose interference performance is good to suppress interference introduced by cable power, and use filters to suppress out-of-band signals, etc (Xu et al. 1995). Although the hardware circuit filtering method can filter out the interference signal, it cannot distinguish between a burst signal and an interference signal, which causes the loss of effective information. Therefore, the software processing methods are often used for image enhancement and interference removal. Most of these methods are used to process the gray-scale image of the spectrum. Common image processing methods for removing radio frequency interference is deleting the interference signal channels or subtracting the mean of its channels. The FFT or wavelet analysis can be used to remove the radio frequency interference, but this method is used to process the gray-scale image of the spectrum in most cases. Although they can enhance the image information, these methods will lose the details of a large number of burst events. In this research, we make use of cutting-edge technical means and a large number of solar radio data, thus a deep learning method is selected to filter out the interference signals.

In recent years, deep learning methods such as multi-modal networks, long short-term memory networks (LSTM), deep-confidence networks, and convolutional neural networks all have good performance in the classification and archiving of solar radio spectrum and identifying burst events (Chen et al. 2015; Yu et al. 2017; Chen et al. 2016, 2017). For example, in terms of astronomical prediction, Huang et al. use convolutional neural networks to predict solar flares (Huang et al. 2018); Sun et al. use the LSTM model to predict the total electron content of the ionosphere through the temporal relationships within the data (Sun et al. 2017); Bikowski M et al. propose a significance-offset convolutional neural network (SOCNN) model for predicting multivariate asynchronous time series in combination with autoregressive models and cyclic neural networks (Binkowski et al. 2018). According to the research results available in the literature, we find that the interference signals to be removed in this paper is similar to the voice signals, and they have certain regularity in time (The time series characteristics mean that the signal is in a certain frequency range, and it shows a certain regular pattern in the process of random variation with time. When this discipline is found, the signal at the next moment can be predicted). Therefore, an algorithm for predicting the RFI signals value in the solar radio burst region that uses a recurrent neural network (RNN) is proposed. Then, according to the numerical characteristic (It means that the interference signals of each frequency channel are regularly changed in a fixed number of values, as exemplified in Sect. 3.3) of the radio interference, the algorithm is improved and digital mapping processing is added to improve the accuracy of the prediction.

2 RELATED THEORETICAL KNOWLEDGE

2.1 The Principle of Recurrent Neural Networks

An RNN accumulates data on the time axis using recursion to memorize information. Figure 1 is the structural diagram of the RNN, where x_t represents the input state at time t, A represents the model processing part of the neural network (it is a repeating module with only one tanh layer), h_t is the state of the hidden layer at time t, and y_t represents the output state at the corresponding time. The matrices of weight coefficients between the layers are represented by w_1, w_2 and w_3. Unlike the traditional neural network, the parameters w_1, w_2 and w_3 for the same location of the RNN at different times are shared, which greatly reduces the number of parameters for the required training. This reduction in parameters lowers the computational load and improves the network training speed.

As can be seen from the above figure, the hidden layer unit h_t at the current moment receives the information of the hidden layer h_{t-1} from the previous moment; the input layer information x_t at the current moment passes data forward. Therefore, the output layer at each moment contains features of the past. The propagation process of the RNN can be expressed as:

$$h_t = f(w_1 x_t + w_2 h_{t-1} + b) \tag{1}$$

$$y_t = f(w_3 h_t + b) \tag{2}$$

where h_{t-1} is the state of the hidden layer at the previous moment; b is the bias term; and f is the relationship of the nonlinear mapping, generally referred to as the activation function.

In theory, the RNN can process a sufficiently long time series. However, the activation function in the RNN often uses the tanh function and the sigmoid function, which leads to the phenomenon that the gradient disappears during the reverse transmission of the error (Yu et al. 2019; Zhang 2017). The disappearing gradient makes the RNN only suitable for processing signals whose time series are short (Lv et al. 2015). In order to fully discover the time series characteristics and obtain more accurate predictions, the signal needs to be fully processed with a long time series (The time series signal for learning and training is approximately 30 s and has at least 4600 frames of data, and the predicted time series signal is approximately 1.5 s and has 150–200 frames of data. One frame of data represents the value of the interference signals for each channel at one point in time. For example, Figure 3 is a solar radio frequency spectrum diagram drawn by a two-dimensional array data. Each row in the array represents data of a single frequency channel as a function of time, and each column represents data of all frequency channels at one point in time. Therefore, one frame of data is equivalent to one column of data in a two-dimensional array. Since the interference signals of a single frequency channel is processed here, one frame refers to the value of a single frequency channel at one moment.). Comparing two special RNN models: both LSTM and gated recurrent unit (GRU) effectively alleviate

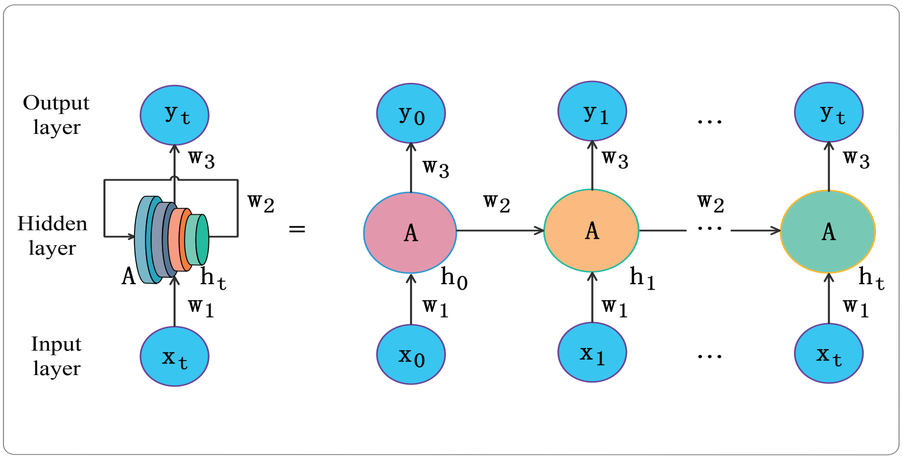

Fig. 1 The structural diagram of the recurrent neural network.

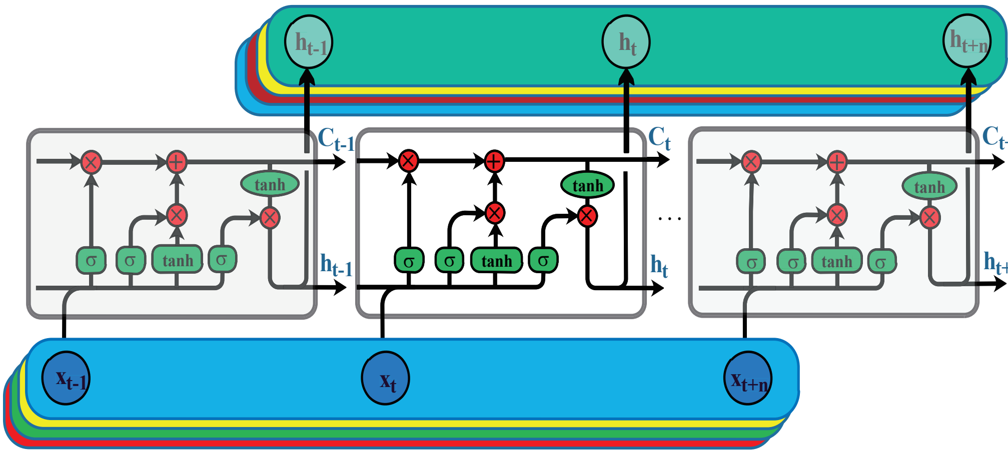

Fig. 2 The structural diagram of the LSTM network.

the problem of gradient disappearance. GRU converges quickly due to fewer parameters. However, in the case of a large data set, LSTM expresses better performance (Chung et al. 2014). Based on the current situation that the amount of data in this paper is sufficient, the LSTM algorithm was finally selected.

2.2 The Principle of the Long Short-Term Memory

Different from the traditional RNN model, the LSTM model replaces the original hidden layer unit with the LSTM cell structural unit. This unit is illustrated in Figure 2 with grey, round-edge rectangles. The information gate is generated by the sigmoid function and is added to the repeatedly linked module. It consists of forgotten gates, input gates, and output gates (Klaus et al. 2016). The function property makes the information passing through each gate carry a parameter that controls the amount of information passed to the current neuron and the amount of information assigned to the next neuron.

The figure above shows the network structure diagram of LSTM. The data transfer process in the figure can be expressed by the following formula (Graves et al. 2013): Forgotten gates:

$$f_t = \sigma(W_{xf}x_t + W_{hf}h_{t-1} + b_f) \tag{3}$$

Input gates:

$$i_t = \sigma(W_{xi}x_t + W_{hi}h_{t-1} + b_i) \tag{4}$$

Output gates:

$$o_t = \sigma(W_{xo}x_t + W_{ho}h_{t-1} + b_o) \tag{5}$$

Cell status of the LSTM:

$$c_t = \tanh(W_{xc}x_t + W_{hc}h_{t-1} + b_c) \tag{6}$$

$$C_t = f_t * C_{t-1} + i_t * c_t \tag{7}$$

Output of the hidden layer:

$$h_t = o_t * \tanh(C_t) \tag{8}$$

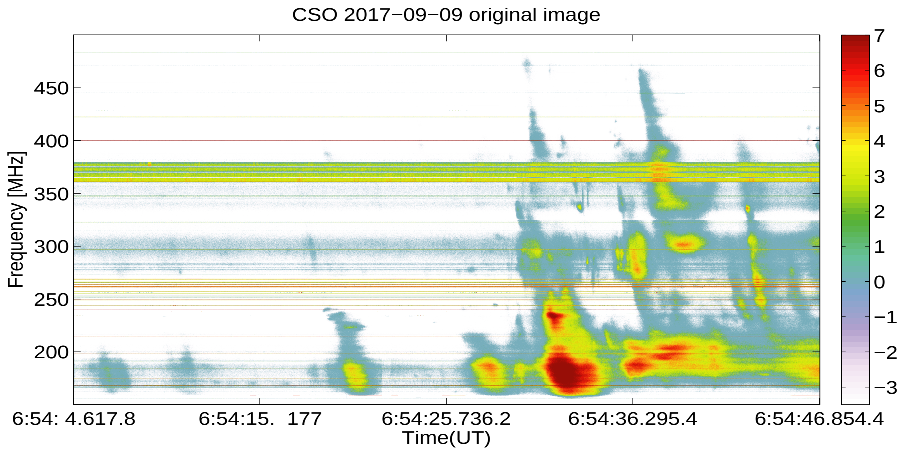

Fig. 3 The intensity map of the 2017–9–9 solar radio burst event. The x-axis represents international time, y-axis are the frequency points (150–500 MHz). In the intensity map, different colors represent different solar emission intensity (the unit is dB) that change over time at different frequencies.

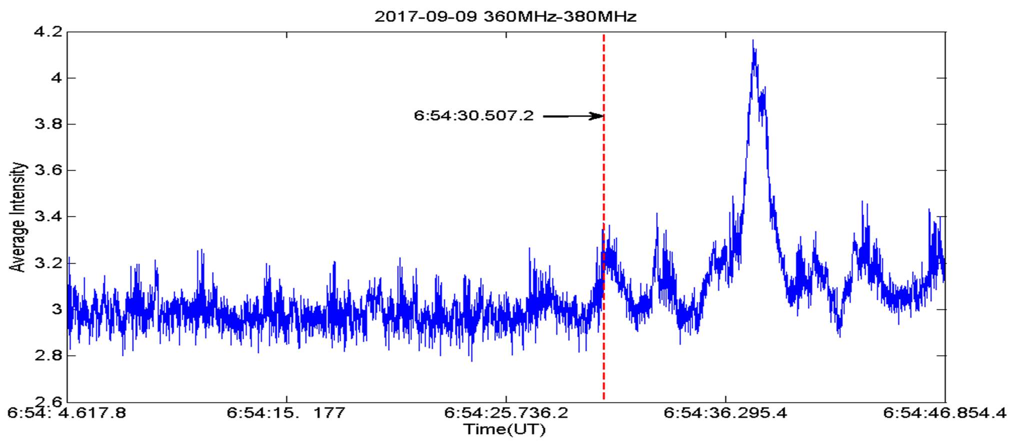

Fig. 4 The initial position map of the 360–380 MHz band burst.

where f, i, and o represent the information of the forgotten gates, the input gates, and the output gates, respectively. W refers to the weight coefficient matrix of the network, b is the bias term, x represents the input of the network, t represents the moment, h is the hidden layer state, c is the state value when the network updates the cell (it is also called the current candidate memory state value), and C is the current memory cell state value of the LSTM network (Li et al. 2018). The three information gates all use the sigmoid function as the activation function, and the tanh function is selected when the memory unit of the network is updated (Miao et al. 2016). The output information of the final hidden layer is related to the output value of the output gates and the current memory cell state value. In addition, compared with RNN, the backpropagation algorithm of the LSTM network not only calculates the error gradient corresponding to the hidden layer state h_t, but also calculates the error gradient of the cell state C_t (Gers et al. 1999).

The application of three information gates in the LSTM network makes the memory cell in the network structure store historical information for a long time. From Equation (7), it can be seen that the LSTM structural unit is composed of two parts, so when the cumulative error is calculated, the result of zero is not present, which alleviates the problem of the gradient disappearance and realizing the long-term memory function.

The GRU is the latest development of the LSTM unit, both variants of the RNN. The GRU reduce the gating signals to two from the LSTM model. They are called an update gate and a reset gate (Dey & Salemt 2017). Although the network structure of GRU is simpler than LSTM, experimental results show that LSTM performance is better than GRU in some cases of sequential prediction (Ergen & Kozat 2017), so this paper still chooses LSTM network structure.

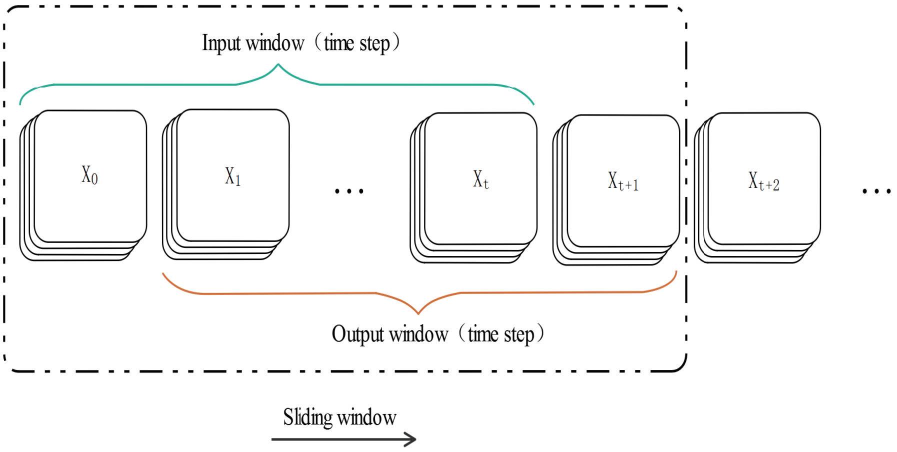

Fig. 5 The schematic diagram of establishing the data set.

3 METHOD AND APPLICATION

3.1 Data Selection

A large solar burst event was observed on 2017 September 9, and the background value of the event in the quiet solar state is zero, so the data of that day are selected for de-interference processing. The data come from the high-frequency solar radio receiver of the Chashan Solar Observatory, with a frequency range of 150–500 MHz, a frequency resolution of 16 kHz, and a time resolution of 10 ms. Because the data received by the data acquisition card are a left-handed circular polarization signal and a right-handed circular polarization signal after the digital polarization synthesis operation, the two signals exist in two data channels. Their values are similar, so only one of the signals, the left-handed circular polarization signal, is selected in this paper for drawing and processing images.

Figure 3 is the intensity graph of the selected burst event. What can be seen from the figure is that there are radio interferences of different intensities in the channels of some frequency points (32 channels correspond to 1 MHz), and the radio channels that affect the event observation need to be filtered out using the method in this paper. For example, the radio channels with a signal strength greater than the intensity of the burst event (215 MHz, 245 MHz, 262 MHz, 400 MHz, etc.) and the frequency bands with a wide interference range (360–380 MHz, about 640 channels).

The interference signals to be processed can be selected by Equation (9).

$$\mathrm{Thresh} \leq \frac{(I(\bar{t})^2)}{\mathrm{Var}(I(t))} \tag{9}$$

where $I(t)$ represents the signal strength value over time in a single channel, $(I(\bar{t})^2)$ and $\mathrm{Var}(I(t))$ represent the mean and standard deviation of all signal strength values within the t period, respectively. The specific size of the threshold for screening the RFI signals, Thresh, can be selected according to the actual situation, and the value of thresh in this article is 40.

In order to more accurately divide the training set in the neural network, it is also necessary to locate the time when the burst event starts. This paper takes the method of averaging the intensity values of multiple channels of the target RFI signals and transforming it into a one-dimensional array that changes with time. Take the radio interference in the 360 MHz-380 MHz band as an example. As shown in Figure 4, when the Sun has not erupted, the average value of each channel is the average value of the RFI signal which experiences little change. However, when the burst events occur, the average value is the average value of the radio interference and the burst value, which is significantly higher than the pure radio interference average. The start time of the burst event handled in this article is the position pointed out by the arrow in Figure 4.

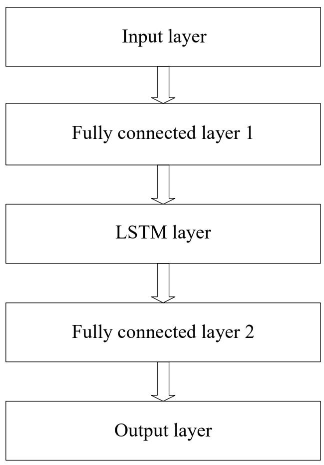

Fig. 6 Network structure diagram.

3.2 Prediction of Radio Interference Signal Value Based on the LSTM Model

3.2.1 Building a data set

The establishment of data sets and network training are the two main parts of deep learning. The purpose of data set standardization is to eliminate the dimensional influence between data, transform data with different units or magnitudes into non-dimensional values, and realize analysis and comparison under the same magnitude. Commonly used methods include normalization. After data standardization, a data set must be established. In order to reduce the amount of network training tasks and improve the accuracy of prediction, the sequence is segmented, and a mapping is considered to be established to find the relationship between the time period and the time period. The process of establishing the data set is shown in Figure 5.

The picture is divided into three parts: input window, output window, and sliding window. A sliding window contains a complete input window and output window. The three windows as a whole slide in the time series, and the sliding unit is one. The input window and the output window contain the same amount of data which is named the time step; this is used as one of the network hyperparameters. The length of the sliding window is related to the time step. Once determined, the time step is determined and also the length of sliding window is determined. In addition, in order to preserve the connection between adjacent sequences as much as possible and improve the accuracy of prediction, the output window and the input window have only one time series interval. Therefore, the sequence values (t-time step + 2) to (t + 1) are predicted from the (t-time step + 1) to (t) sequence information.

3.2.2 Establishment of LSTM network and prediction of radio interference values

The LSTM network built in this paper is divided into five layers (Fig. 6): input layer, fully connected layer 1, LSTM layer, fully connected layer 2, and output layer. Firstly, the data set is transformed into the required dimension of the network after entering the first fully connected layer. Then, the LSTM layer automatically extracts a series of timing features through its internal loop operation. Then, the output feature vector enters the second full connection layer. Finally, the network outputs the predicted radio interference value. As can be seen from Section 3.2.1, the last frame of data output by the network is the radio value for the next moment of prediction.

In order to improve the network performance and enhance the learning ability of the model, it is generally preferred to increase the number of network layers and the number of nodes in the layers. However, increasing the depth of the model not only increases the time of the network training, but also causes over-fitting that reduces the final prediction accuracy. Therefore, this section of the experiment selects four LSTM layers to extract features, and the number of nodes is 25 (the parameters are based on the experimental results in Table 1). In addition, the back propagation through time (BPTT, the principle of BPTT algorithm is consistent with back propagation, BP. The difference is that when calculating the error term, BPTT is necessary to calculate the error in a time direction to update the weight between hidden layers. The BP algorithm consists of two processes: forward propagation of the signal and back propagation of the error.) algorithm and the gradient descent algorithm are selected to complete the training of network weights. An MSE loss function and a mini-batch based stochastic gradient descent optimizer are added according to the training results.

After the model training is completed, it enters the prediction stage. In order to test the performance of the network, the test data (the value of the known pure radio interference signal position) is used for prediction. The network structure is adjusted by comparing the results using the original data of the corresponding position. Since the position of the radio interferences value to be predicted is unknown, a step-by-step prediction method is required for prediction, i.e., the predicted value is added to the next input for a second prediction every time. Figure 7 shows a comparison of the 100-frame radio interference signal predicted by a single channel with the original data. The blue line indicates the test set data and the red line indicates the prediction result. It can be seen from the figure that the discipline of the predicted value and the actual value change with time is about the same, but the numerical values are different. The reason is that the step-by-step prediction method introduces errors and the prediction ability of the model decreases over time.

3.3 Prediction of Radio Interference Value Based on Improved LSTM Network

As can be seen from the previous section, the step-by-step prediction method continuously introduces errors, which affects the overall prediction results. By observing the characteristics of the radio interference signal, we find that the data of each channel have only a fixed number of values. Therefore, adopting the method of adding a digital mapping is proposed to reduce the error and improve the accuracy of prediction. For example, Figure 8 shows the original sequence diagram and the histogram of 6000 frames of data from four randomly selected channel. Figure 8 shows that the values of these channels have

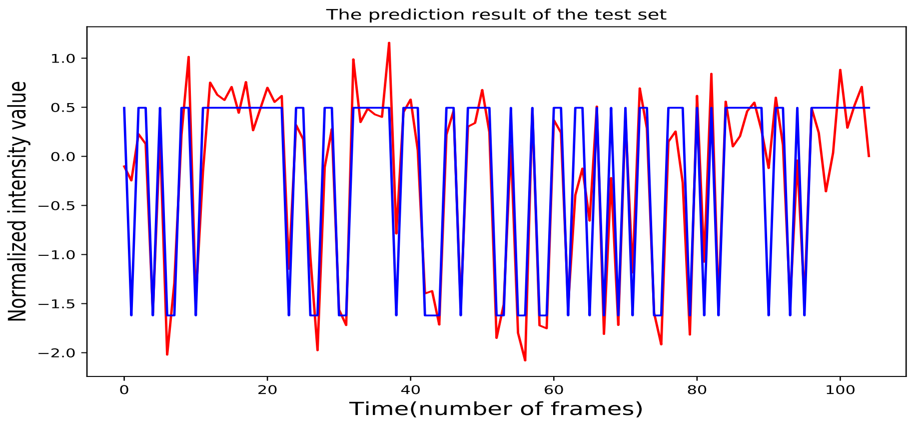

Fig. 7 The prediction result of the test data (100-frame radio interference signal).

a different number of categories, ranging from 2 to 5. Therefore, the values appearing in the sequence can be treated as different classes, and the prediction problem is converted into a classification problem. The predicted value is the value with the highest predicted probability in the classification. As long as the predicted trend is correct, the accuracy of the predicted value at that moment is 100%. This avoids the problems illustrated in Figure 7 (We processed the data entering the network based on the Z-score normalization method. Therefore, the data shown in Fig. 7 are different from those in Fig. 8).

3.3.1 Building a data set

The establishment of the dataset in this section is basically the same as that in Section 2.2. Data preprocessing and a sliding window are required to extract the data. The difference is that the size and position of the output window in the sliding window has changed, and the data in the window is labeled. The schematic diagram of the changed data set is shown in Figure 9. The output window contains only one frame of data and is located next to the end of the input window. Therefore, the sequence values of $(t + 1)$ are predicted from (t-time step + 1) to (t) sequence information, while the sliding window still slides only one frame at a time. After obtaining the value by segmentation sliding, the mapping of the time segment (input window) to the time point (output window) is generated. Then, the classification corresponding to the time point data is converted into the label of the corresponding time segment.

The data in the sliding window are labeled by one-hot encoding, which converts the number of categories into binary numbers. The N-type values are encoded with an N-bit register to ensure that only one valid position per class is activated and marked as one; the other locations are marked as zero. For example, the values of the radio interference signal in Figure 8(b) have four categories, so $N = 4$.

3.3.2 Prediction of the radio interference value based on the digital mapping method

The network structure used in this section is similar to Section 3.2. However, for better classification the dropout function is added to the model to avoid over-fitting in the network, and the loss function is changed to the softmax cross-entropy function (Hu et al. 2018; Spurek et al. 2017), which is more suitable for classification operations. The learning and updating of weights utilizes the Adam algorithm (Chang et al. 2019) for the adaptive learning rate optimization.

Considering that this paper needs to process 768 channels of RFI signals, it means we should call 768 network models for prediction. The hyperparameters involved in this paper have time step length “time_step”, the number of hidden layer node “unit”, the number of trainings entering the network each time “batch_size”, network depth “num_layer”, and learning rate “lr”, etc. The workload is heavy when each channel adjusts the hyperparameters to obtain the optimal model, since the training process for a single channel takes approximately 30 minutes, this means that each modification of the hyperparameter must be retrained for 30 minutes, while the five hyperparameters of the 768 channels require at least 5 * 768 * 0.5 = 1920 h. Therefore, a large number of experiments are first used to screen out a set of optimal hyperparameters for the learning, training, and prediction of the 768 models.

The sample set for screening the optimal hyperparameters consists of 10 channels of data that are randomly selected from the 768 RFI signal channels. In order to determine the appropriate training set, experiments with samples of 3000, 6000 and 9000 frames were carried out,

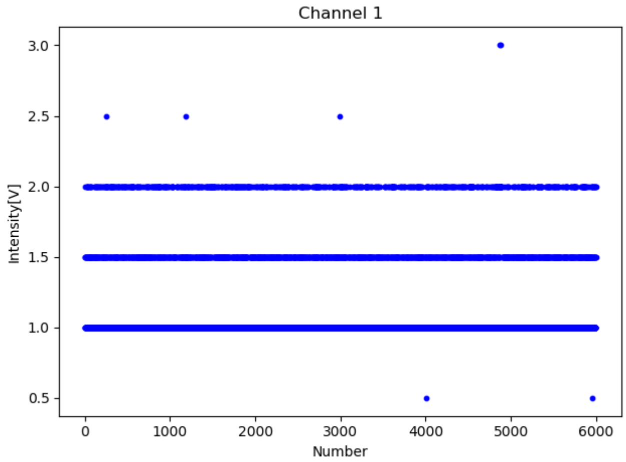

(a) Scatter plot of channel 1

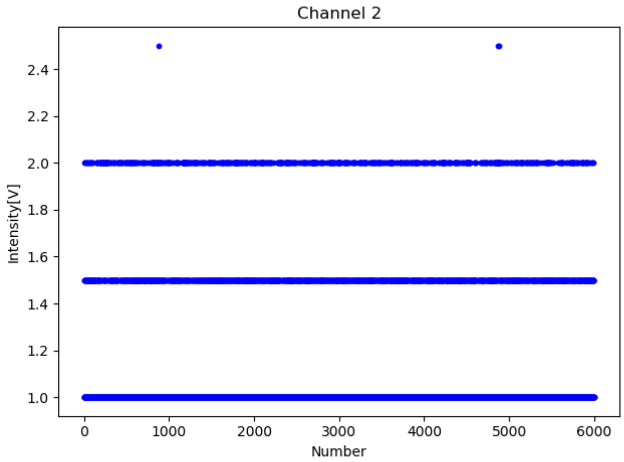

(b) Scatter plot of channel 2

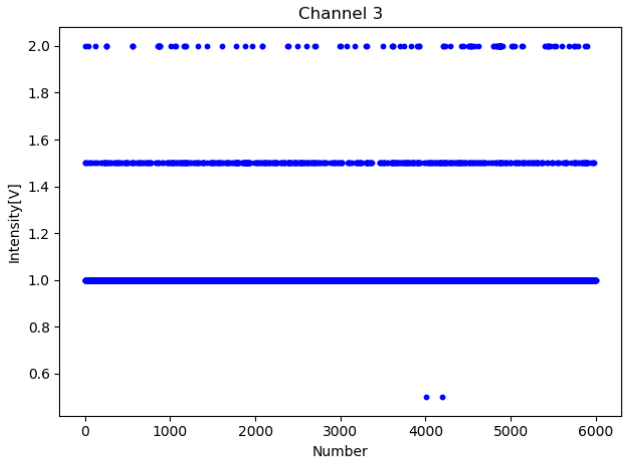

(c) Scatter plot of channel 3

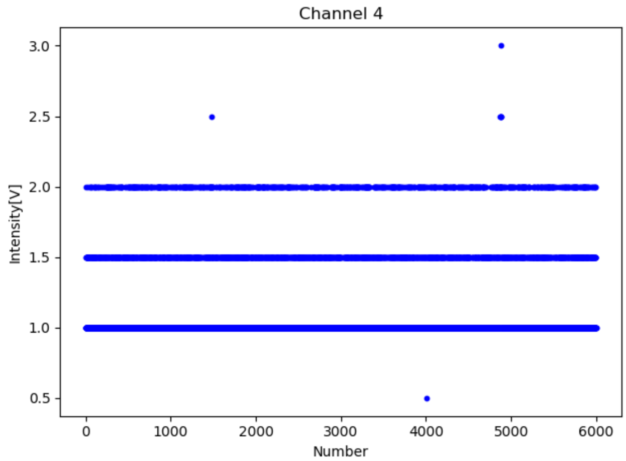

(d) Scatter plot of channel 4

Fig. 8 The original sequence diagram of four random channels.

Table 1 Experimental Results of Parameter Adjustments - 3000 Frames

num_layer	unit	accuracy	the accuracy after adding dropout
2	20	0.731	0.735
2	30	0.728	0.731
3	20	0.736	0.74
3	30	0.72	0.735
4	20	0.746	0.75
4	30	0.740	0.734
5	20	0.738	0.744
5	30	0.73	0.747

Table 2 Experimental Results of Parameter Adjustments - 9000 Frames

num_layer	unit	accuracy	the accuracy after adding dropout
2	20	0.706	0.71
2	30	0.710	0.7
3	20	0.704	0.72
3	30	0.714	0.725
4	20	0.726	0.733
4	30	0.730	0.72
5	20	0.733	0.735
5	30	0.738	0.732

and the data was divided into a test set (5%) and a training set (95%). The idea of dichotomy is used here. First try to use the smaller number of frames 3000 and the larger number of frames 9000, because the data of the observation system is about 10 000 frames per unit stored in the disk array. Through experiments, it is found that too small an amount of data and too much data are not conducive to network training. The experimental results are as Table 1 and Table 2.

From the data recorded in the table, it is found that the accuracy of 9000 frames of data is lower than that of 3000 frames of data. It can be estimated that the appropriate number of frames must be between 3000 and 9000, so it is better to determine 6000 as the appropriate number.

The experimental results of some parameter adjustments are presented in Table 3. The effects of network depth, the number of hidden layer nodes, and dropout function on network prediction are studied under the

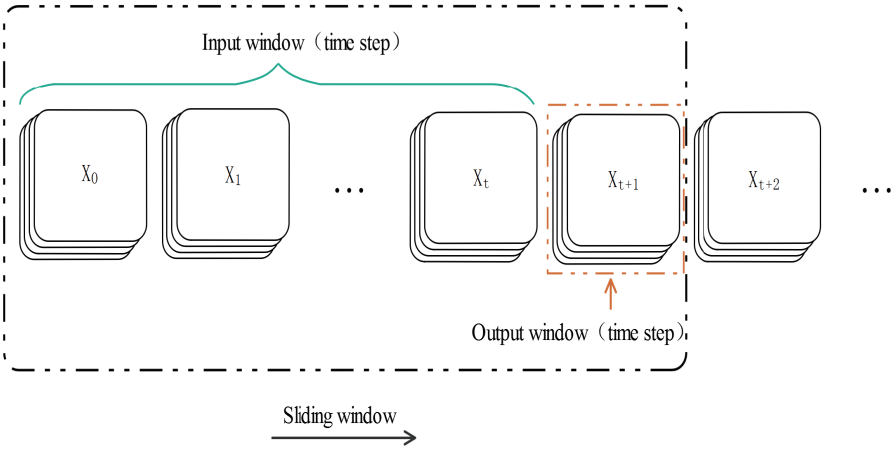

Fig. 9 The schematic diagram of data set establishment based on digital mapping.

Table 3 Experimental Results of Parameter Adjustments - 6000 Frames

num_layer	unit	accuracy	the accuracy after adding dropout
2	20	0.796	0.800
2	25	0.768	0.804
2	30	0.800	0.801
2	35	0.776	0.808
3	20	0.784	0.808
3	25	0.704	0.800
3	30	0.764	0.778
3	35	0.796	0.796
4	20	0.776	0.796
4	25	0.800	0.812
4	30	0.780	0.800
4	35	0.800	0.800
5	20	0.448	0.784
5	25	0.752	0.760
5	30	0.748	0.796
5	35	0.764	0.808

Table 4 Experimental Results of Parameter Adjustments: Learning Rate and time_step (Four Layers and 25 Nodes)

the learning rate (lr)	time_step	accuracy
0.1	15	0.804
0.1	20	0.802
0.1	25	0.804
0.1	30	0.800
0.1	35	0.804
0.01	15	0.804
0.01	20	0.808
0.01	25	0.796
0.01	30	0.792
0.01	35	0.792
0.001	15	0.804
0.001	20	0.812
0.001	25	0.804
0.001	30	0.708
0.001	35	0.776

condition of a fixed learning rate (lr=0.001) and time step (time_step=35). The numerical values of the learning rate and time step are one of the results randomly selected from the exhaustive way of traversing all the parameter combinations.

As can be seen from the table, it is not the deeper the better for the network. When the number of nodes is 20 and the network has five layers, the accuracy of the prediction is only 44.8%. This is because the network structure has been over-fitting with the deepening of the network. The prediction accuracy is improved to 78.4% after adding the dropout function. The prediction accuracy after adding the dropout function is consistently higher than that without adding the function, which demonstrates the value of adding the dropout function. From the table, a set of hyperparameters with the highest prediction accuracy rate is selected; these are the four-layer network with 25 nodes. These values are used to continue the experiment for the learning rate and time step. According to the results of Table 4, finally, the learning rate in the optimal hyperparameter is determined to be 0.001, and the time_step is 20.

4 THE RESULTS AND ANALYSIS OF THE INTERFERENCE SIGNAL SUPPRESSION

4.1 Prediction of Radio Interference Value Based on Improved LSTM Network

The actual value of the radio interference signal to be processed in this paper is unknown in the burst position. In order to verify the effect of using the method in this paper and the performance of the digital mapping method in the filtering process, we establish the event simulation. The two methods mentioned in Section 2 are used to process and analyze the event simulation.

According to the principle that signals can be linearly added, the simulation data are superimposed with the pure burst data and the pure RFI data. The pure burst data are composed of the data from 6:52:23.461.7–6:52:27.131.7 (international time) and 225 – 240 MHz on 2019 September 9, which has 471 channels and 351

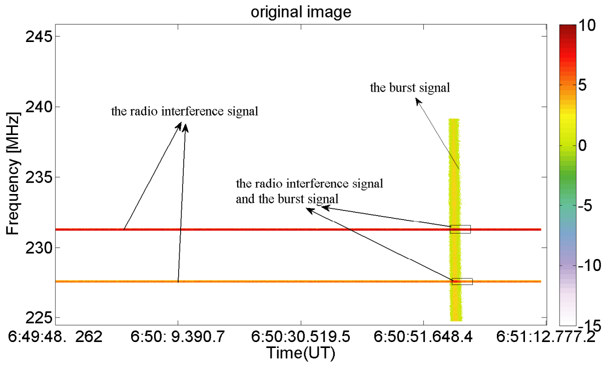

Fig. 10 The intensity map of the simulation event.

frames. The pure radio data consists of the data on 2017 September 9 at 6:49:48.262–6:51:12.808.6 and 248.85 – 249 MHz, which has six channels and 8064 frames. Keeping the frequency band of the burst event unchanged and the time of the radio interference unaltered, the pure RFI signal value is superimposed to 227.5 MHz, and then it is doubled to the position of 231 MHz. Consequently, we obtain a simulation burst event with a frequency range of 224 – 247 MHz and a time range of 6:49:48.262–6:51:12.808.6. This is shown in Figure 10.

Firstly, the LSTM network is used to train the six selected channels of radio interference data and predict the RFI signal value of the burst position. Then, the predicted burst position data is subtracted to obtain the processing result graph shown in Figure 11. What can be seen from the processed intensity map is that some visible interference signals remain in the burst event, and the results are not very satisfactory.

The RFI signal is processed using the LSTM network based on the digital mapping method. Table 5 shows the accuracy of the prediction results of the six channels after classification and labeling. Although some channels' accuracy is as low as 0.5 (The reason for the low accuracy is that the more the number of label classifications, the more complicated the signal variation law, so we need to train with more data to get higher accuracy.), the average accuracy of the overall data can reach 74.33%. The final intensity map is shown in Figure 12. The RFI signals in the burst area are mostly removed, and the observation of the event is not obscured. Comparing the result with original image without RFI (Fig. 11(c)) and Figure 11(b), the filtering effect of the LSTM network (Fig. 12) based on the digital mapping method is significantly better than that of the general LSTM network.

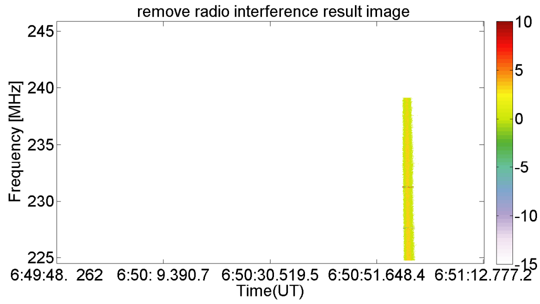

(a) Image of removing RFI based on the LSTM network

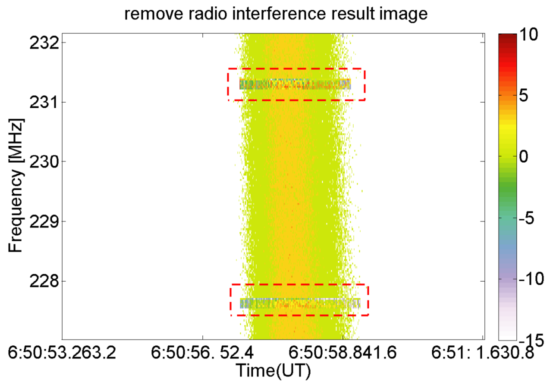

(b) Image of zoom into the residuals for Fig. 11(a)

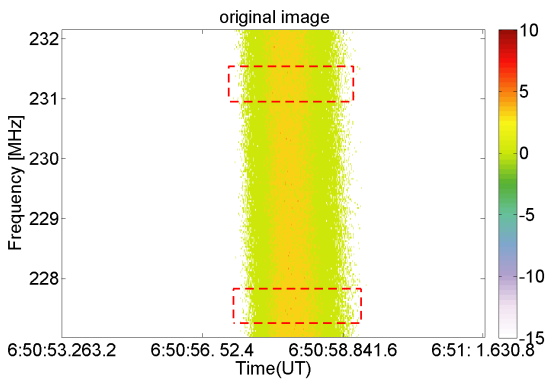

(c) Original image without RFI

Fig. 11 Image of removing RFI based on the LSTM network and Original image without RFI.

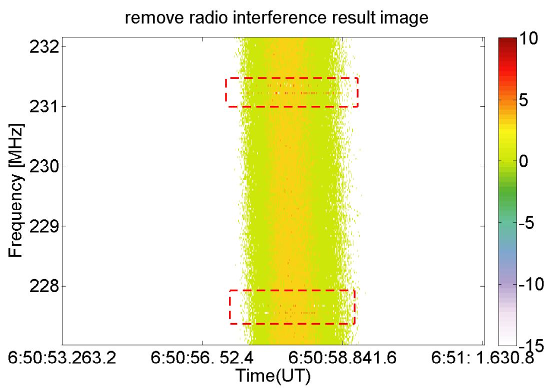

Fig. 12 The intensity map of removing RFI based on the improved LSTM network.

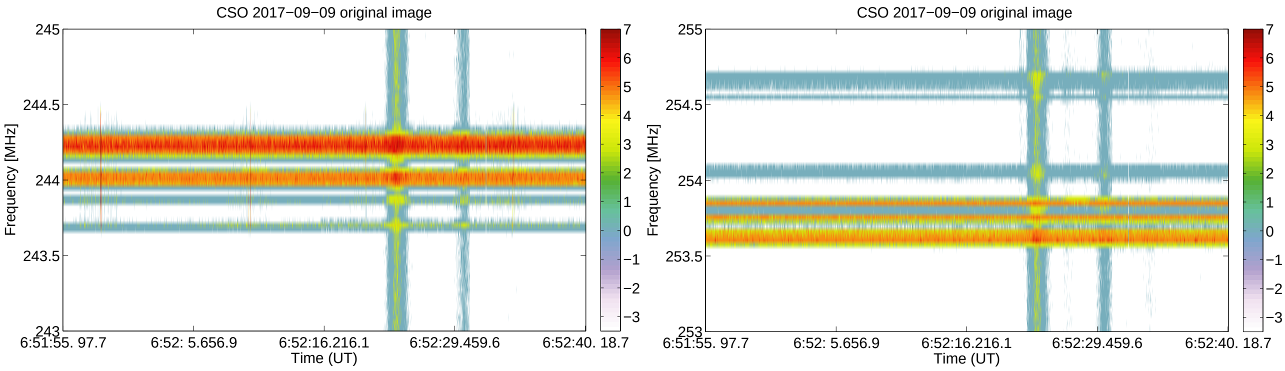

(a) Original image of the 244 MHz (b) Original image of the 253 MHz

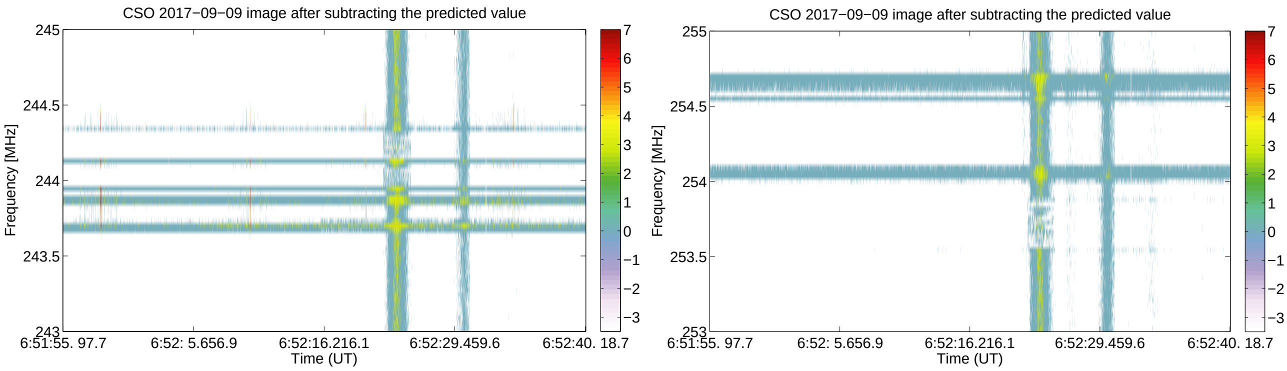

(c) Processed image of the 244 MHz (d) Processed image of the 253 MHz

Fig. 13 Images in 244 MHz and 253 MHz.

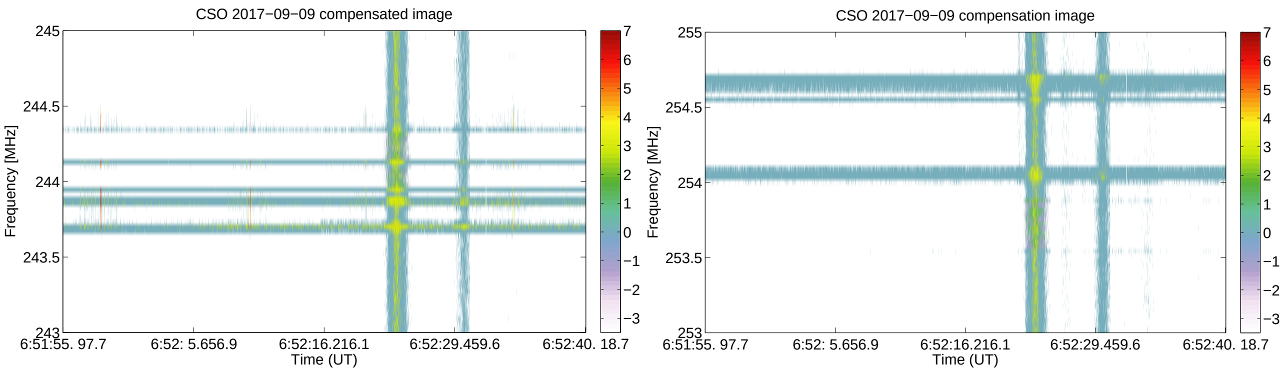

(a) Compensated image in 244 MHz (b) Compensated image in 253 MHz

Fig. 14 Compensated images in 244 MHz and 253 MHz.

Table 5 The Predictive Accuracy Using the Improved LSTM Network

RFI signal channel	1	2	3	4	5	6
number of labels	3	4	4	3	3	2
accuracy	0.78	0.50	0.60	0.74	0.87	0.97

4.2 Analysis of Actual Event Processing Results

4.2.1 Compensation for actual event processing

The simulation event superimposes the pure RFI signal value and the intensity value of the pure burst event, which conforms to the principle that signals can be linearly added. However, we found that the processing result is excessively suppressed. The actual RFI signal value of the burst position is smaller than the predicted value, and a part of the burst information is removed when the radio predicted value is subtracted from the original value of the burst position. Figure 13 is the result of the radio interference processing of a small burst event that occurs two minutes before the event in Figure 3. It can be seen that when the improved LSTM network is used to predict the radio interference value near 244 MHz and 253 MHz and process the event, there is a gap between the actual effect and the theoretical result. This result is due to a sharp increase in the signal strength when the solar radio bursts. Once the signal is amplified, the amplifier may work in a nonlinear region, resulting in the attenuation of the collected data. In addition, the process of the solar burst also affects the radio interference signal to some extent. Therefore, the two signals no longer satisfy the linear additivity of the signal, and the processing needs to be compensated in some way.

The system used to collect data is a high-frequency resolution system with an average of 32 frequency channels corresponding to 1 MHz. The solar burst events usually occupy a large bandwidth in the frequency domain and are distributed in hundreds of frequency channels of the system. The high frequency resolution makes the values in adjacent frequency channels similar, which makes it possible to compensate for the processing results using burst data from adjacent radio interference signal channels. The compensation calculation formula is as follows:

$$F(a,k) = \frac{f(a) + k * g(b)}{2} \tag{10}$$

where $F(a,k)$ is the compensated value, $f(a)$ is the value of the area where the interference signal is over-attenuated, $g(b)$ is the value of the adjacent channel of the interference signal, k is the coefficient, and a and b represent different frequency channels. The coefficient k is selected according to the actual situation. Figure 14(a), (b) are the compensated images of Figure 13(c), (d), respectively. The compensated images better preserve the effective information of the burst event while removing the radio interference.

4.2.2 *The processing result of actual event*

The actual burst event whose time range is 6:54:4.617.8–6:54:46.854.4 is Figure 3 in Section 2.1, and the prediction time starts at 6:54:30.507.2. In order to further prove the superiority of the proposed method, the ordinary image processing method is firstly adopted for the burst event to remove the radio interference signals. We choose the method of subtracting the mean of the single channel radio interference signals. To avoid the influence of the burst value on the channel mean, we select the 500 frames of data around the event 6:54:15 to calculate the channel mean, then the time and frequency resolution are reduced by six times and 16 times, respectively. The results are shown in Figure 15. It can be seen from the figure that the burst continuity of the wide red frame portion covered by the radio interference signals is destroyed, and the effective information is removed. Therefore, this section uses the improved LSTM network to process the radio interference

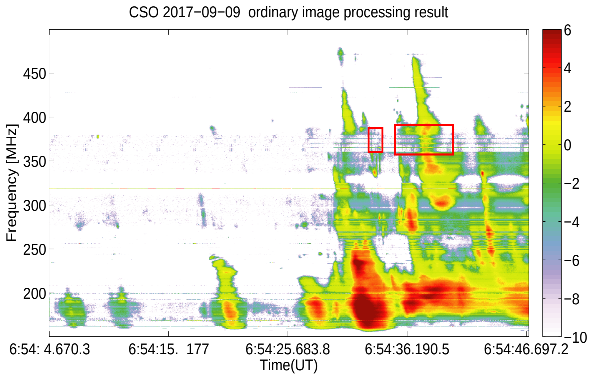

Fig. 15 The intensity map of the ordinary image processing results.

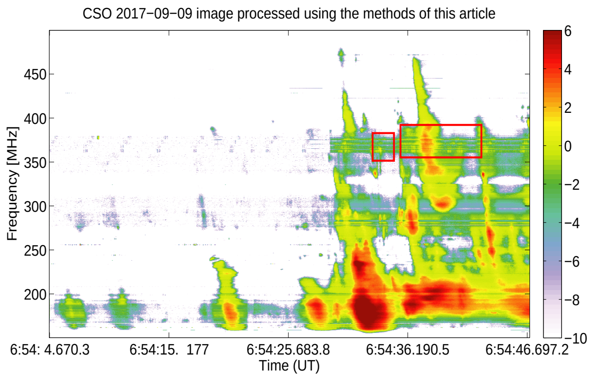

Fig. 16 The intensity map of the combination processing results (improved LSTM and compensation).

signals in the outburst location; the interference signals that are not related to the burst event and the weaker interference signals are processed by subtracting the mean of the corresponding channel's value.

Figure 16 is the processed result of using the method that combines the improved LSTM network and compensation, where k is taken as 20. In comparison with the original image and Figure 15, we can see that not only small-scale burst events between 250 MHz and 300 MHz can be clearly displayed in the spectrum, but also the burst event that is originally covered in the red frame can be clearly observed. Furthermore, the continuity of the burst events in frequency is also preserved.

In order to more intuitively compare the two processing methods and further demonstrate the superiority of using the methods herein to remove solar radio interference, some details of Figures 15 and 16 are shown simultaneously in Figures 17, 18, and 19. Part of the spectrogram allows for a clear view of the processing of each radio interference (multiple channels). Figures 17(a), 18(a) and 19(a) are the result of processing using the improved LSTM method, Figures 17(b), 18(b) and 19(b) are the result of the processing of the ordinary image

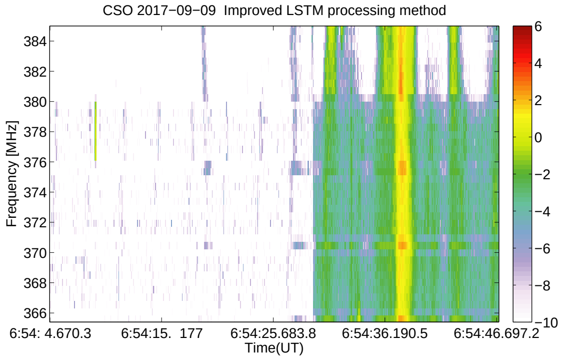

(a) Improved LSTM processing method

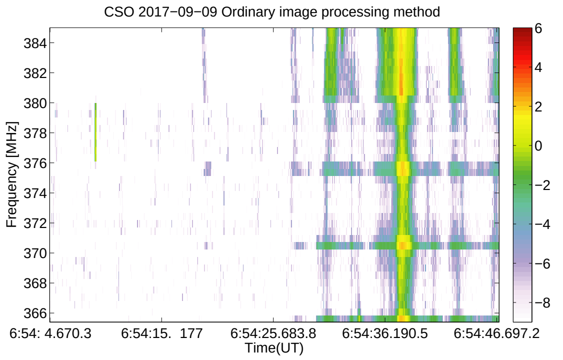

(b) Ordinary image processing method

Fig. 17 365–385 MHz interference radio processing results.

processing method. The information in Figures 17(a), 18(a) and 19(a) is more reserved than that in Figures 17(b), 18(b) and 19(b) about the burst signal.

In summary, the intensity of the interference signal at the burst is unknown and the accuracy of the network prediction cannot be determined. However, according to the experimental results, it can be found that regardless of the frequency band occupied by the interference signal, the proposed method can be used to process the radio interference signal. Then, the Binkowski et al. (2018) Autoregressiveprocessed part is compensated by using the degree burst information. In this paper, the interference signal is finally removed while the burst information is retained as much as possible.

5 CONCLUSIONS

In this paper, a novel method of predicting the radio interference signals in the solar radio spectrum based on the LSTM network is proposed. According to the characteristics of the RFI signals, the long time series signals are mapped to a certain time step to find the relationship between time periods. The predicted radio trend is similar to the original data, but the predictions are not accurate enough. In view of this situation, we propose an improved LSTM network based on the digital mapping

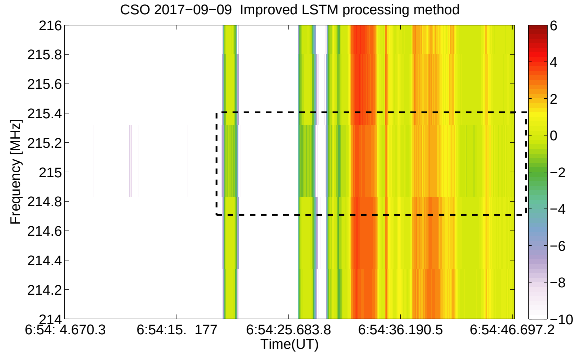

(a) Improved LSTM processing method

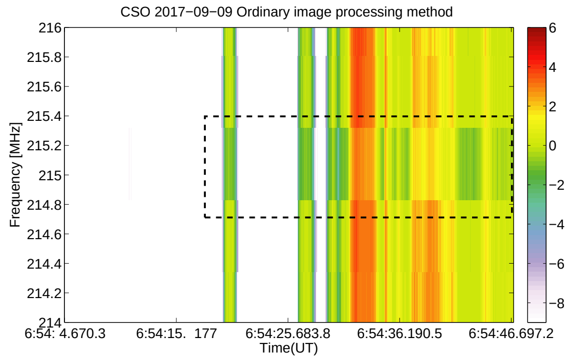

(b) Ordinary image processing method

Fig. 18 215 MHz interference radio processing results.

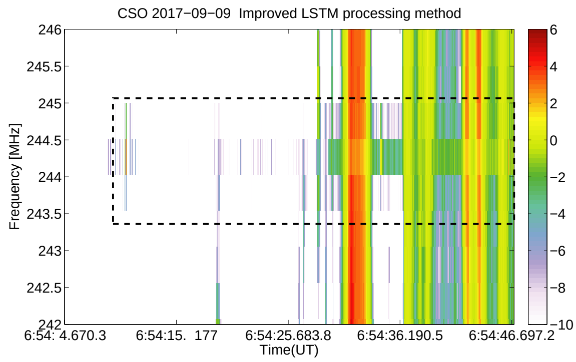

(a) Improved LSTM processing method

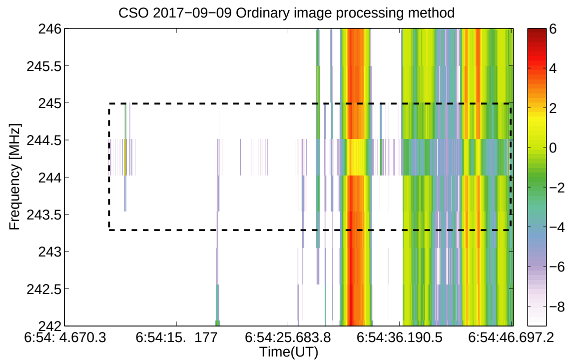

(b) Ordinary image processing method

Fig. 19 244 MHz interference radio processing results.

method. Before entering into the network, the single frequency channel radio data should be classified. First, we establish the mapping from time periods to time points. Then, the corresponding time period label is established, which is conducted according to the classification of the output time point. The improved LSTM network greatly improves the accuracy of the prediction results and provides a possibility of lossless filtering of the solar spectrum.

However, to remove the radio interference to achieve better results and to ensure a higher prediction accuracy, the use of this method has certain limitations, because the data in this paper are received by the high-resolution spectrum analyzer. There are fewer data classifications in each frequency channel, and the data of adjacent frequency channels do not change significantly. If the prediction of low-resolution data is performed, the accuracy of prediction will be reduced because the data classification is increased.

The method mentioned in this paper still has room for optimization: it takes substantial time to train the 768 networks in this event. A GPU can be used to train and predict multiple networks at the same time to improve work efficiency. In addition, although the errors caused by stepwise prediction are effectively suppressed by the methods in this paper, the error itself cannot be avoided. Finally, more periodic data can be added to support the analysis and extraction of additional valid features, and the use of step-by-step predictions can be avoided.

References

Binkowski, M., Marti, G., & Donnat, P. 2018, in International Conference on Machine Learning, 580

Chang, Z., Zhang, Y., & Chen, W. 2019, Energy, 187, 115804

Chen, S., Xu, L., Ma, L., et al. 2017, in 2017 IEEE International Conference on Multimedia & Expo Workshops (ICMEW), IEEE, 198

Chen, Z., Ma, L., Xu, L., Tan, C., & Yan, Y. 2016, Multimedia Tools & Applications, 75, 2859

Chen, Z., Ma, L., Xu, L., Weng, Y., & Yan, Y. 2015, in 2015 IEEE International Conference on Systems, Man, and Cybernetics, IEEE, 1035

Cheng, R. 2018, The Digital Polarization Solar Radio Spectrum with High Resolution, PhD Thesis, Shandong University

Chung, J., Gulcehre, C., Cho, K., & Bengio, Y. 2014, arXiv e-prints, arXiv:1412.3555

Dey, R., & Salemt, F. M. 2017, in 2017 IEEE 60th International Midwest Symposium on Circuits and Systems (MWSCAS), IEEE, 1597

Ergen, T., & Kozat, S. S. 2017, IEEE Transactions on Neural Networks and Learning Systems, 29, 3772

Gers, F. A., Schmidhuber, J., & Cummins, F. 1999, in Learning to Forget: Continual Prediction with LSTM, 9th International Conference on Artificial Neural Networks: ICANN '99 (IET), 850

Graves, A., Jaitly, N., & Mohamed, A.-r. 2013, in 2013 IEEE Workshop on Automatic Speech Recognition and Understanding, IEEE, 273

Hu, K., Zhang, Z., Niu, X., et al. 2018, Neurocomputing, 309, 179

Huang, X., Wang, H., Xu, L., et al. 2018, ApJ, 856, 7

Klaus, G., Srivastava, R. K., Koutnłk, J., et al. 2016, IEEE Transactions on Neural Networks & Learning Systems, 28, 2222

Li, Z., He, D., Tian, F., et al. 2018, arXiv e-prints, arXiv:1806.02988

Lv, Y., Duan, Y., Kang, W., Li, Z., & Wang, F. 2015, IEEE Transactions on Intelligent Transportation Systems, 16, 865

Miao, Y., Li, J., Wang, Y., et al. 2016, in 2016 IEEE International Conference on Acoustics, Speech and Signal Processing (ICASSP), IEEE, 2284

Spurek, P., Tabor, J., & Byrski, K. 2017, Expert Systems with Applications, 72, 49

Sun, W., Xu, L., Huang, X., et al. 2017, in 2017 International Conference on Machine Learning and Cybernetics (ICMLC), 2, IEEE, 340

Xu, Z.-C., Wu, H.-A., Xu, F.-Y., & Cha, D.-Y. 1995, Chinese Astronomy and Astrophysics, 19, 399

Yu, L., Qu, J., Gao, F., & Tian, Y. 2019, Shock and Vibration, 2019, 1

Yu, X., Xu, L., Ma, L., et al. 2017, in 2017 IEEE International Conference on Multimedia & Expo Workshops (ICMEW), IEEE, 519

Zhang, Y. 2017, Activation Function Oriented RNN Algorithm Optimization, PhD Thesis, Zhejiang University